







Article

A Reversible Protonic Ceramic Cell with Symmetrically Designed $\text{Pr}_2\text{NiO}_{4+\delta}$ -Based Electrodes: Fabrication and Electrochemical Features

Artem Tarutin ^{1,2}, Julia Lyagaeva ^{1,3}, Andrey Farlenkov ^{3,4}, Sergey Plaksin ⁴,
Gennady Vdovin ¹, Anatoly Demin ^{1,3} and Dmitry Medvedev ^{1,5,*}

¹ Laboratory of Electrochemical Devices Based on Solid Oxide Proton Electrolytes, Institute of High Temperature Electrochemistry, Yekaterinburg 620137, Russia; vanomass333@gmail.com (A.T.); yulia.lyagaeva@ya.ru (J.L.); vdovin@ihete.uran.ru (G.V.); a.demin@ihete.uran.ru (A.D.)

² Institute of New Materials and Technologies, Ural Federal University, Yekaterinburg 620002, Russia

³ Institute of Chemical Engineering, Ural Federal University, Yekaterinburg 620002, Russia; a.farlenkov@yandex.ru

⁴ Laboratory of Solid State Oxide Fuel Cells, Institute of High Temperature Electrochemistry, Yekaterinburg 620137, Russia; plaksin@ihete.uran.ru

⁵ Graduate School of Economics and Management, Ural Federal University, Yekaterinburg 620002, Russia

* Correspondence: dmitrymedv@mail.ru; Tel.: +7-343-3623202

Received: 23 November 2018; Accepted: 26 December 2018; Published: 31 December 2018



Abstract: Reversible protonic ceramic cells (rPCCs) combine two different operation regimes, fuel cell and electrolysis cell modes, which allow reversible chemical-to-electrical energy conversion at reduced temperatures with high efficiency and performance. Here we present novel technological and materials science approaches, enabling a rPCC with symmetrical functional electrodes to be prepared using a single sintering step. The response of the cell fabricated on the basis of P–N–BCZD|BCZD|PBN–BCZD (where BCZD = $\text{BaCe}_{0.5}\text{Zr}_{0.3}\text{Dy}_{0.2}\text{O}_{3-\delta}$, PBN = $\text{Pr}_{1.9}\text{Ba}_{0.1}\text{NiO}_{4+\delta}$, P = Pr_2O_3 , N = Ni) is studied at different temperatures and water vapor partial pressures ($p_{\text{H}_2\text{O}}$) by means of volt-ampere measurements, electrochemical impedance spectroscopy and distribution of relaxation times analyses. The obtained results demonstrate that symmetrical electrodes exhibit classical mixed-ionic/electronic conducting behavior with no hydration capability at 750 °C; therefore, increasing the $p_{\text{H}_2\text{O}}$ values in both reducing and oxidizing atmospheres leads to some deterioration of their electrochemical activity. At the same time, the electrolytic properties of the BCZD membrane are improved, positively affecting the rPCC's efficiency. The electrolysis cell mode of the rPCC is found to be more appropriate than the fuel cell mode under highly humidified atmospheres, since its improved performance is determined by the ohmic resistance, which decreases with $p_{\text{H}_2\text{O}}$ increasing.

Keywords: PCFCs/PCECs; Ruddlesden-Popper phases; symmetrical cells; proton-conducting electrolytes

1. Introduction

Solid oxide systems with predominant protonic transport are considered as advanced applied materials for the energy sector. A particular interest is associated with their utilization as proton-conducting electrolytes in protonic ceramic cells (rPCCs), reversible solid oxide cells that are used to convert different types of energy with high efficiency and no harmful impact [1–5]. Compared with conventional solid oxide cells with oxygen-ionic electrolytes, rPCCs are able to operate at reduced temperatures due to their high proton mobility and low activation energy [6–8]. These advantages may feasibly lead to their commercialization in the near future [9]. Therefore, carrying out the

necessary applied and fundamental research in this field, as well as developing new approaches for the optimization of the relevant technological and electrochemical processes, are among highly relevant current trends.

Recently, many efforts have been made to simplify technological processes involved in the fabrication of solid oxide devices based on oxygen-ionic or proton-conducting electrolytes [10,11]. One of these efforts consists in designing electrochemical cells having symmetrical electrodes [12] as an efficient strategy for reducing fabrication costs. Here, the economic benefit lies in minimizing the number of functional materials used. Moreover, this strategy can help to resolve problems associated with thermal incompatibility and electrochemical degradation if the latter has a reversible nature [13,14]. However, materials for symmetrical electrodes preparation must satisfy a number of requirements, such as excellent electrochemical activity in both reduced (Red) and oxidized (Ox) conditions, as well as appropriate phase and thermal behavior under RedOx cycling. As a rule, only a limited series of materials can be used for this purpose, including Ti-, Fe-, Cr- and Mn-based oxides with simple or double perovskite structures [12].

Although the utilization of symmetrical solid oxide fuel cells based on oxygen-ionic electrolytes has been intensively studied in the past few years [13–17], the application of this strategy to PCCs is only at the beginning of its development. In the present work, we propose to use a $\text{Pr}_2\text{NiO}_{4+\delta}$ -based oxide in symmetrical functional layers for a rPCC. In contrast to the previously mentioned simple or double perovskite, a layered structure of praseodymium nickelate is substituted under reducing atmospheres to complete Ni reduction and formation of a Ni– Pr_2O_3 cermet (Figure 1) with good electrocatalytic properties [18,19]. Along with the symmetrical electrode application and reversible operation mode, the close thermal expansion coefficients (TECs) of $\text{Pr}_2\text{NiO}_{4+\delta}$ - and $\text{Ba}(\text{Ce},\text{Zr})\text{O}_3$ -based materials [20,21] allow a one-step sintering procedure to be used. According to the literature analysis, a single temperature processing step is a highly attractive approach for reducing the fabrication costs; in particular, this strategy has recently been adopted for the production of PCCs [8,22,23]. However, in these works the anode and cathode layers consisted of different functional materials, which can cause a mechanical misbalance leading to the deformation of whole cells following their sintering. Utilizing the same component for both functional electrode layers minimizes the possible strain, representing significant benefits in technological aspects, as well as the in terms of the quality of the target product.

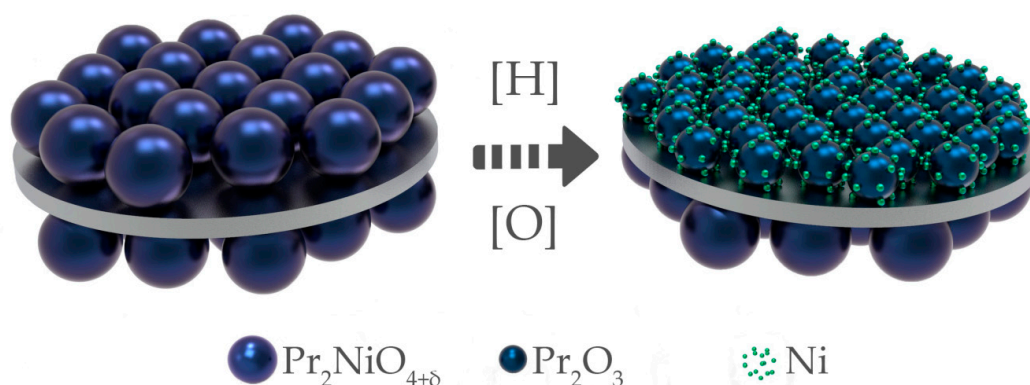


Figure 1. Principal scheme of a symmetrically designed PCC and $\text{Pr}_2\text{NiO}_{4+\delta}$ reduction with the formation of a Ni-based cermet.

2. Materials and Methods

2.1. Preparation of Materials

The protonic ceramic cell (PCC) was fabricated from three functional materials, including $\text{BaCe}_{0.5}\text{Zr}_{0.3}\text{Dy}_{0.2}\text{O}_{3-\delta}$ (BCZD) as a proton-conducting electrolyte layer (EL), its mixture with nickel oxide as a substrate for supporting fuel electrode layer (SFEL) and $\text{Pr}_{1.9}\text{Ba}_{0.1}\text{NiO}_{4+\delta}$ (PBN) as a basis for functional oxygen (FOEL) and functional fuel (FFEL) electrode layers.

The BCZD and PBN powders were obtained using the citrate-nitrate synthesis method described in detail in our previous works [24,25].

2.2. Characterization of Materials

The phase structure of the individual materials (BCZD, PBN) and their mixture (1:1 at ratio) calcined at 1350 °C for 3 h was studied by X-ray diffraction analysis (Rigaku D/MAX-2200VL [26]). The scans were performed under $\text{CuK}\alpha_1$ radiation between 20° and 80° with a scan step of 0.02° and a scan rate of 3° min^{-1} .

The morphology of the ceramic samples and multilayered cell was studied using scanning electron microscopy (SEM) and energy dispersive X-ray (EDX) analyses on a Tescan Mira 3 LMU microscope with an Oxford Instruments INCA Energy X-MAX 80 spectrometer [26].

Thermogravimetric (TG) technique (Netzsch STA 449 F3 Jupiter) was employed to study reduction behavior of the PBN powder.

Conductivity measurements were carried out in air and wet H_2 atmospheres using a convenient 4-probe DC current method (Zirconia-318 measurement station).

2.3. Fabrication of the PCC

The single-phase BCZD was mixed with NiO and starch (pore former) in a weight ratio of 3:2:1 to prepare the powder for the SFEL, while BCZD was mixed with PBN and pore former in a weight ratio of 4:1:1 to be used as FOEL and FFEL. The mixing stages were performed using a Fritsch Pulverisette 7 planetary ball mill with the following conditions: zirconia milling balls, acetone media, 500 rpm for 0.5 h. The corresponding powders were mixed with an organic binder (butadiene rubber in acetone/benzene solvent) and rolled using a Durtson rolling mill to fabricate the functional films having the required thicknesses. These films were then co-rolled with each other (tape-calendering method), adjusted by ~30 μm for the raw EL, ~20 μm for the raw FOEL and FFEL and ~800 μm for the raw SFEL. The green multilayered NiO-BCZD|PBN-BCZD|BCZD|PBN-BCZD structure was slowly (1 °C min^{-1}) heated up to 900 °C to decompose and remove organic residue, then heated further to 1350 °C at a heating rate of 5 °C min^{-1} , sintered at this temperature for 3 h and cooled to room temperature at a cooling rate of 5 °C min^{-1} .

2.4. Characterization of the PCC

The fabricated PCC with an effective electrode area of 0.21 cm^2 was characterized at a temperature range of 600–750 °C under reversible operation (bias changes from 0.1 to 1.5 V with a step of 25 mV). The volt-ampere dependences and impedance spectra were obtained using a complex of Amel 2550 potentiostat/galvanostat and Materials M520 frequency response analyzer. To evaluate the electrode response, hydrogen as a fuel and air as an oxidant were humidified to varying degrees. The target water vapor partial pressure values were set by passing the corresponding atmospheres through a water bubbler heated to certain temperatures. The impedance spectra were obtained across a frequency range of 10^{-2} – 10^5 Hz at a perturbation voltage of 25 mV and were then analyzed utilizing the methods of equivalent circuits (Zview software) and distribution of relaxation times (DRT, DRTtools core of the Matlab software [27]).

3. Results and Discussion

3.1. $\text{Pr}_{1.9}\text{Ba}_{0.1}\text{NiO}_{4+\delta}$ Functionality

To assess the applied prospect of PBN as electrodes for PCCs, its properties were comprehensively studied (Figure 2).

This material is characterized by a high chemical compatibility with the proton-conducting electrolytes based on $\text{Ba}(\text{Ce,Zr})\text{O}_3$ (Figure 2a), since the high-temperature treatment results in maintaining the basic structures for both phases, although a small amount of NiO exists at the same

time (this impurity phase is also visible at the interface regions, see the Ni-element distribution map on Figure 3c). According to our best knowledge, we have used the highest temperature (1350 °C), at which chemical interactions of cerate-zirconates and nickelates were studied. Such excellent results in phase stability can be explained by the fact that $\text{Pr}_2\text{NiO}_{4+\delta}$ is doped with barium, that compensates the Ba-concentration difference between two components and, therefore, diminishes a degree of chemical interaction [28,29].

As it is shown in Figure 2b, the PBN material in a powder state starts to reduce at 300 °C, when interstitial (and a part of lattice-site) oxygen is gradually removed [30]; this nickelate is almost completely decomposed at temperatures above 600 °C, which is in line with the following simplified reaction: $\text{Pr}_2\text{NiO}_{4+\delta} \rightarrow \text{Pr}_2\text{O}_3 + \text{Ni}$, see Figure 1.

Conductivity of the as-prepared ceramic sample in air atmosphere differs from one of the reduced samples in wet hydrogen by more than four orders of magnitude (Figure 2d). It can be concluded that the reduced sample represents a mixture of $(\text{Pr,Ba})_2\text{O}_3$ and Ni with a mole ratio of 2:1. In other words, the total conductivity is determined by oxide phases, since no continuous high conductive metallic framework is formed under such a reduction. Nevertheless, Ni-particles appear during the exsolution procedure (Figure 2c), which is found to be a remarkable factor in electrode processes improvement [31]. According to Figure 2c, a certain part of Pr_2O_3 is transformed to $\text{Pr}(\text{OH})_3$, but this hydroxide is formed at relatively low temperatures only (under cooling of the sample in static air), when Pr_2O_3 chemisorbs steam of air. This is confirmed by the fact that the total weight change of PBN under full reduction is equal to 95.2% ($\delta_{\text{RT}} = 0.17$, $4 + \delta_{1000\text{ °C}} = 2.95$; see Figure 2b) corresponding with the formation of 0.95 mole of Pr_2O_3 and 0.1 mole of BaO at 1000 °C. Otherwise, if $\text{Pr}(\text{OH})_3$ was formed during the reduction procedure, the overall weight change should amount to 96.1%. This level corresponds to $\delta_{\text{RT}} = -0.07$ ($4 + \delta_{1000\text{ °C}} = 2.95$), which is in disagreement with that reached for $\text{Pr}_2\text{NiO}_{4+\delta}$, which has a close composition, $\delta = 4.23\text{--}4.25$ [32,33].

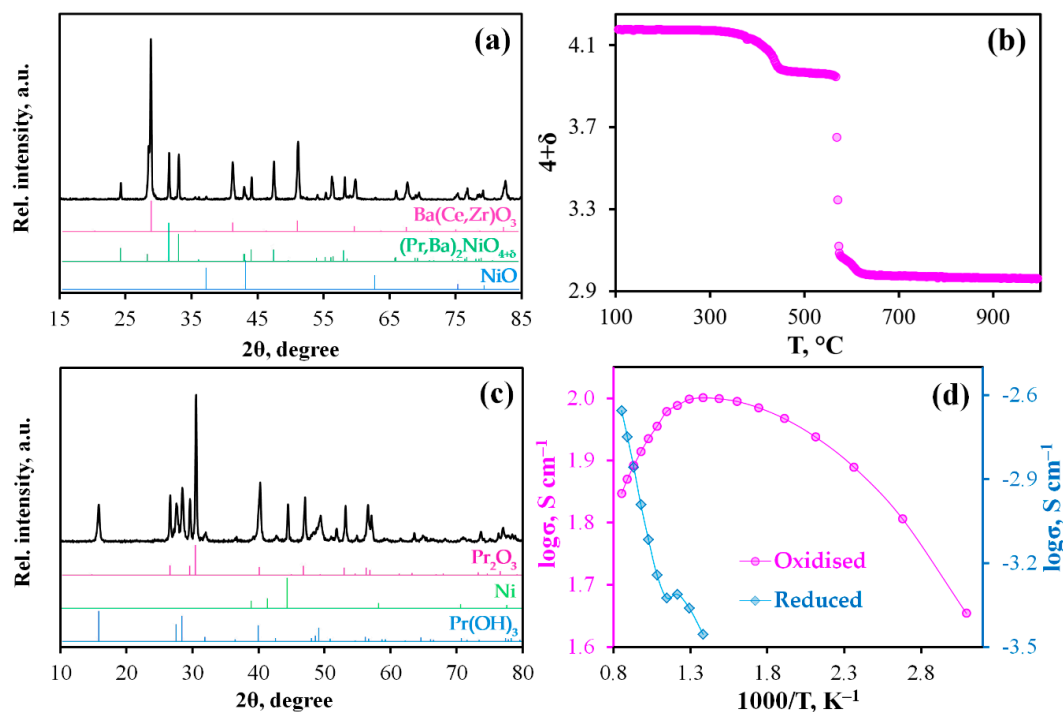


Figure 2. (a) XRD pattern of the BCZD – PBN mixture calcined at 1350 °C for 5 h; (b) TG curve obtained under reduction of the PBN powder in 50% H_2/N_2 atmosphere; (c) XRD pattern of the reduced product of the PBN material (after TG analysis); (d) Conductivity of the PBN samples in oxidizing and reducing atmospheres.

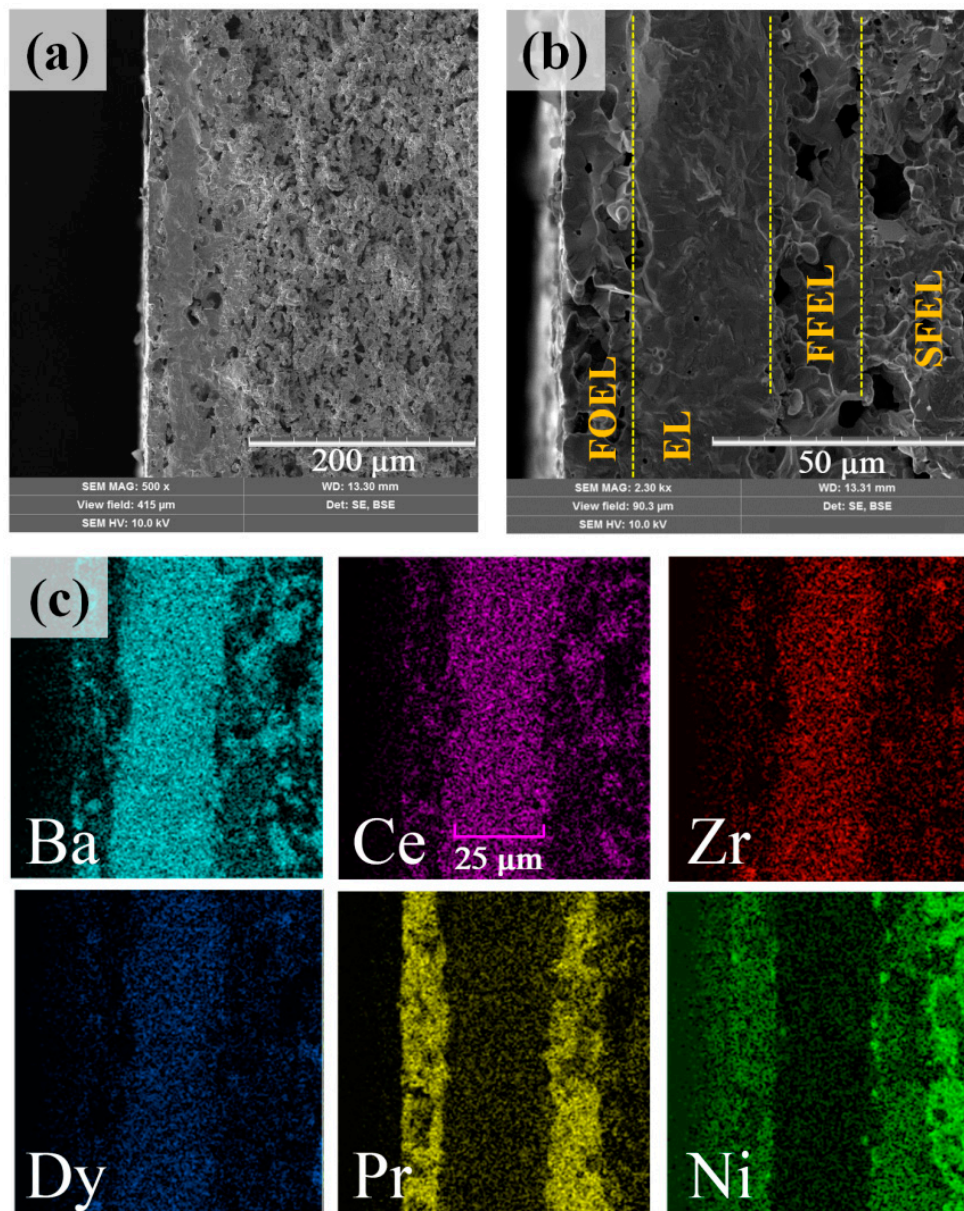


Figure 3. Cross-section images of the fabricated rPCC at different magnification (a,b) and maps of the elements distribution (c).

3.2. Microstructural Features

The PCC fabricated using the one-step sintering procedure shows a well-organized, multi-layered structure without any visible deformation, material delamination or cracks (Figure 3a). The obtained results can be explained by the excellent thermal compatibility of the $\text{Ln}_2\text{NiO}_{4+\delta}$ -based ($\text{Ln} = \text{La}, \text{Pr}, \text{Nd}$) materials with $\text{Ba}(\text{Ce}, \text{Zr})\text{O}_3$ proton-conducting electrolytes, especially the low chemical expansion in contrast to that of many electrode materials having perovskite-related structures [34,35].

The resulting thickness of the FOEL, EL and FFEL are estimated to be about 15, 25 and 17 μm , respectively (Figure 3b), while the total PCC thickness is equal to 700 μm . The porosity of SFEL evaluated using ImageJ software amounts to 40 ± 5 vol.%; the porosity of the functional electrodes does not exceed 20% (measured on the individually prepared pellets with the same composition, $\text{BCZD}:\text{PBN}:\text{starch} = 4:1:1$), indicating their strong sintering behavior despite 20 wt.% of pore former used.

According to EDX analysis (Figure 3c), elements are evenly distributed and do not show significant interdiffusion, forming clearly separated interphase boundaries. This also supports the conclusion regarding the chemical compatibility of materials used, at least at a sintering temperature of 1350 °C.

3.3. Volt-Ampere Dependences and Related Properties

The operability of the reversible PCC is shown in Figure 4a. In the current-free mode, this cell generates open circuit voltages (OCV) of 1.076, 1.051, 1.006 and 0.979 V at 600, 650, 700 and 750 °C, respectively. These values are somewhat lower than those theoretically predicted, which amount to 1.135, 1.126, 1.118 and 1.109 V, respectively. Since this cell maintains gas-impenetrability (measured at room temperature under 10^{-3} atm/1 atm of total gas pressures gradient), the most likely reason for the observed differences is non-ionic conduction of the BCZD electrolyte. Indeed, both BaCeO₃- and BaZrO₃-based materials demonstrate meaningful electron conductivity in oxidizing conditions at high temperatures [36,37]. Regarding the BCZD electrolyte, its ionic transference numbers (t_i) estimated as a ratio of its ionic conductivity measured in wet H₂ to the total conductivity measured in wet air only reached 0.78, 0.62, 0.50 and 0.44 at 600, 650, 700 and 750 °C [38]. It should be noted that these t_i values were determined for the samples in system with unseparated gas space, when all the samples' sides were in contact with the same atmosphere. In the case of PCC, the electrolyte membrane separates two gas spaces. Therefore, one subsurface of the membrane exhibits predominant proton transport, while another one features mixed ionic-electronic transport. Therefore, the resulting (or average) ionic transference numbers, $t_{i,av}$, should be much higher than t_i . The exact $t_{i,av}$ values under OCV conditions can be calculated as follows [39]:

$$t_{i,av} = 1 - \frac{R_O}{R_O + R_p} \left(1 - \frac{E_{meas}}{E} \right), \quad (1)$$

where, R_O and R_p are the ohmic and polarization resistances of the PCC, while E_{meas} and E are the measured and theoretically predicted potentials. As can be seen, this equation includes the parameters related to the resistances of the functional materials, which can be separated using the impedance spectroscopy method. The separation procedure will be described in Section 3.4 and the calculation of $t_{i,av}$ values shown in Section 3.6.

The PCC yields such maximal power densities (P_{max}) as 305, 360, 395 and 430 mW cm⁻² at 600, 650, 700 and 750 °C, respectively (Figure 4b,d). In electrolysis cell mode of operation, the maximal current densities reach about 640, 780, 950 and 1070 mA cm⁻² ($U = 1.5$ V) at the corresponding temperatures and about 295, 405, 535 and 690 mA cm⁻² under conditions close to the thermoneutral mode ($U_{TN} \approx 1.3$ V, Figure 4c,d). This mode is determined by the thermodynamic parameter of the resulting reaction occurring in the rPCC (Equations (2) and (3)) and corresponds to the conditions when the cell is in thermal equilibrium. More precisely, the rPCC consumes heat when the bias is lower than U_{TN} and, conversely, produces heat when the bias exceeds U_{TN} .



$$U_{TN} = \frac{-\Delta H}{zF}. \quad (3)$$

Here, ΔH is the molar enthalpy of reaction (2), z is the number of participating electrons ($z = 2$) and F is the Faraday constant.

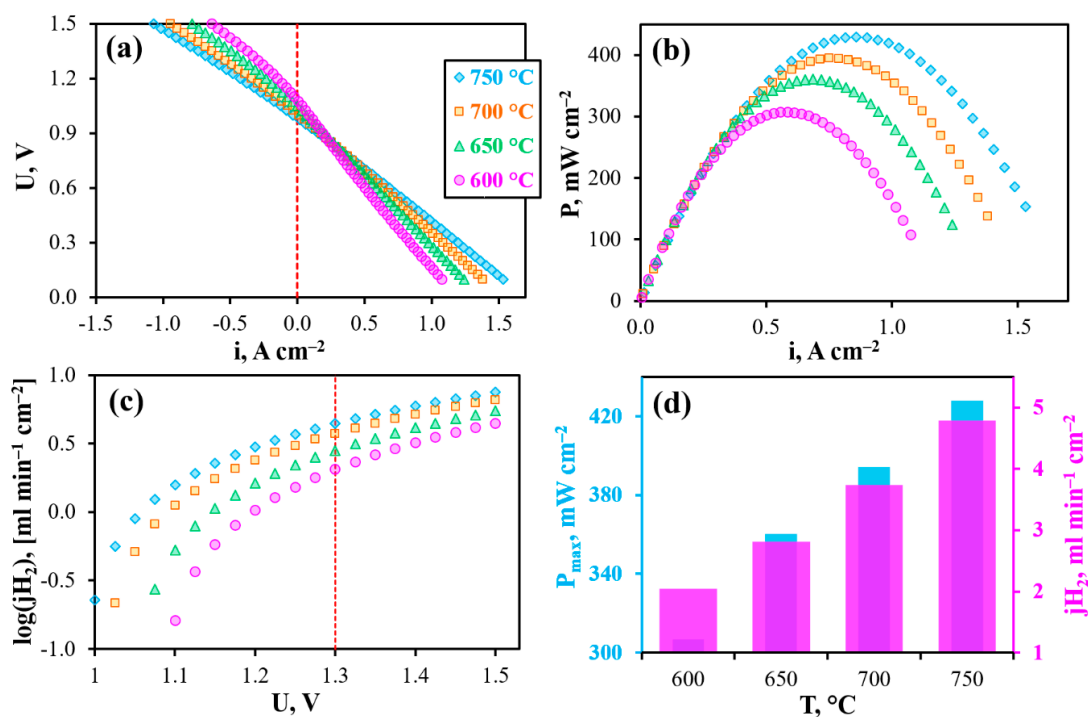


Figure 4. Reversible operation of the PCC at different temperatures under 3% $\text{H}_2\text{O}/\text{H}_2$ –3% $\text{H}_2\text{O}/\text{air}$ conditions: volt-ampere curves (a), power density characteristics (b), maximal achievable hydrogen flux density (c), maximal power density and hydrogen flux density at $U = 1.3$ V depending on temperature (d).

3.4. Analysis of Impedance Data

First, the PCC's functionality was characterized under OCV mode using EIS analysis (Figure 5). As can be seen from these data, all the obtained impedance spectra consist of two clearly separated arcs, corresponding to low- and high-frequency processes. In order to correlate these partial processes with the corresponding resistances, the experimental results were fitted by the model lines originated from the used $L-R_0-(R_1Q_1)-(R_2Q_2)$ equivalent circuit scheme. Here, L is the inductance associated with cables, wires and their junctions, R_0 is the ohmic resistance of the electrolyte membrane, R_1 and R_2 are the resistances of low-(I) and high-(II) processes, Q_1 and Q_2 are the corresponding constant phase elements. Two fitting results (presented in Figure 5 as examples) confirm a good agreement between experimental and model data, implying the success of the used scheme.

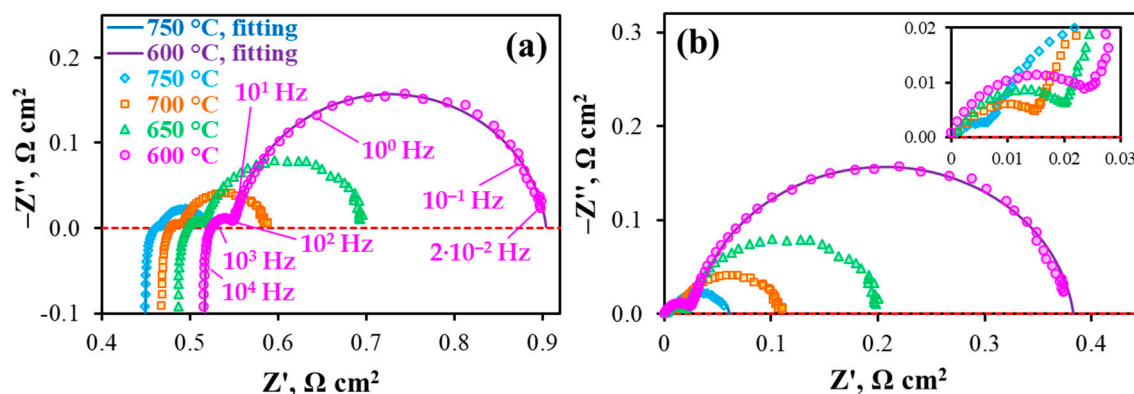


Figure 5. Impedance spectra of the PCC at different temperatures under 3% $\text{H}_2\text{O}/\text{H}_2$ –3% $\text{H}_2\text{O}/\text{air}$ and OCV conditions: original spectra (a) and ones obtained after subtracting the ohmic resistance (b).

According to the fitting procedure, the R_O , R_1 , R_2 parameters, along with the polarization resistance of the electrodes ($R_p = R_1 + R_2$) and total resistance of the PCC ($R_{total} = R_O + R_p$), were successfully determined, as shown in Figure 6. With increasing temperature, the total polarization resistance of the PCC decreases from 0.90 to 0.52 $\Omega \text{ cm}^2$ (Figure 6a); at the same time, this resistance is determined by the ohmic component (Figure 6b), the contribution of which varies between 57 and 86%. Two factors contribute to this result: the rather high thickness of the electrolyte used (25 μm) and the excellent electrochemical properties of the electrodes, despite their fairly low porosity. The total polarization resistance of the electrodes decreases from 0.39 $\Omega \text{ cm}^2$ at 600 $^\circ\text{C}$ to 0.07 $\Omega \text{ cm}^2$ at 750 $^\circ\text{C}$ and is regulated by the R_2 level, which contributes to amounts to 91% and 71%, respectively.

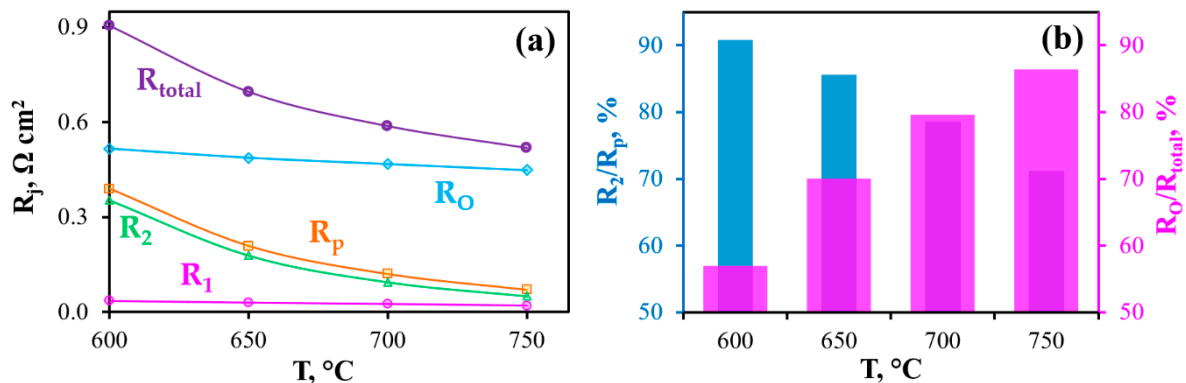


Figure 6. (a) Constituent resistances (R_j) of the total resistance of the PCC depending on temperature; (b) Contributions of Process II in the total polarization resistance and the ohmic resistance in the total resistance of the PCC at different temperatures.

All the constituent resistances have a thermo-activated nature with different activation energies, E_a (see Appendix A, Figure A1). The Process II exhibits the highest E_a value, indicating a strong correlation with temperature; conversely, the E_a level of Process I is lower than that of Process II by ~ 3 times. The E_a level of the PCC's total resistance is quite low (0.37 eV), since it is regulated by the predominant influence of the ohmic resistance with the lowest E_a . Two important conclusions are supported by the obtained data:

- (1) The low E_a for the ohmic resistance is an indirect evidence of proton behavior, since protons migrate much more easily than massive oxygen-ions [40,41];
- (2) The slight temperature behavior of the total resistance of the PCC is a characteristic feature of the cells, corresponding to the condition of $R_p < R_O$. Therefore, their output parameters (as shown in Figure 4d) also change slightly with temperature variation.

In order to evaluate the prospect of utilizing the $\text{Pr}_2\text{NiO}_{4+\delta}$ -based material as symmetrical electrodes, Processes I and II were thoroughly analyzed by calculating the capacitance/frequency values and utilizing the DRT method.

The values for the capacitance and frequency characteristics (at the top of the arcs) were estimated from the impedance spectra fitting as follows:

$$C_j = (R_j \cdot Q_j)^{1/n_j} \cdot R_j^{-1}, \quad (4)$$

$$f_j = (R_j \cdot Q_j)^{-1/n_j} \cdot (2\pi)^{-1}, \quad (5)$$

where $j = 1$ or 2 , n_j is the exponent factor [42,43].

Process I semicircles are characterized by the characteristic capacitances of 3.6×10^{-3} – 6.4×10^{-3} F cm^{-2} and characteristic frequencies of 4×10^2 – 6×10^2 Hz ; these values reach 8.5×10^{-1} – 9.0×10^{-1} F cm^{-2} and 4×10^{-1} – 4×10^1 Hz , respectively, for the semicircles of Process II. These results are

also supported by the DRT data (Figure 7). As can be seen, Processes I and II correspond to the medium- and low-frequency stages, respectively. In detail, the first rate-determining step can be attributed either to the surface charge-transfer phenomenon [44] or to ionic diffusion at the electrode [45] with direct participation of proton charge carriers due to having a low E_a value (Figure A1). Although low values are achieved for this stage at the estimated frequencies, it should be noted that the electrodes (at least, the oxygen one) represent quite a dense structure for an electrolytic component, which might provide proton transportation. Due to high E_a and C_2 values, the second rate-determining (and dominating) step corresponds to sluggish gas-diffusion and adsorption of electrochemically-active components [46,47], which correlates with the mentioned low porosity of the electrodes.

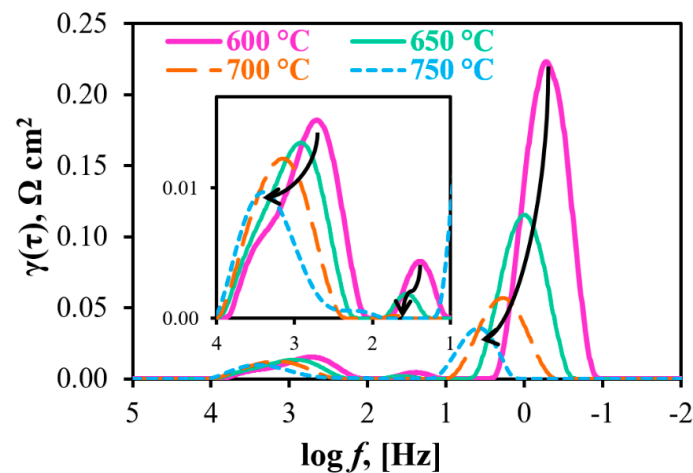


Figure 7. DRT results for the obtained impedance spectra (see details in Figure 5a).

Along with these two steps, the high-resolution DRT method [48,49] gives an additional peak around tens of Hz (see inset in Figure 7). The partial polarization resistance corresponding to this peak (R_1') does not exceed 0.005 and 0.002 $\Omega \text{ cm}^2$ (below 1.5% of R_p) at 600 and 650 $^\circ\text{C}$, respectively; therefore, it cannot be resolved under convenient impedance data analysis by equivalent circuits. Considering its mediate frequencies and strong dependence on temperature, such a peak can likely be associated with the dissociation of adsorbed molecules [46,47].

Summarizing, the symmetrically-formed electrodes yield a promising performance of the PCC regardless of their low-porous microstructure. Moreover, the obtained results are in line with characteristics for similar PCC electrolyte and oxygen electrode materials (Table 1, [50–53]).

Table 1. Polarization behavior of the $\text{Pr}_2\text{NiO}_{4+\delta}$ -based electrodes of PCCs under OCV mode of operation ¹: T is the temperature, R_p is the total polarization of the electrodes.

Electrolyte	Electrode	T, $^\circ\text{C}$	R_p , $\Omega \text{ cm}^2$	Ref.
$\text{BaCe}_{0.5}\text{Zr}_{0.3}\text{Dy}_{0.2}\text{O}_{3-\delta}$ (BCZD)	$\text{Pr}_{1.9}\text{Ba}_{0.1}\text{NiO}_{4+\delta}$ -BCZD	600	0.39	This work
		700	0.12	
$\text{BaCe}_{0.7}\text{Zr}_{0.1}\text{Y}_{0.2}\text{O}_{3-\delta}$ (BCZY1)	$\text{Pr}_{1.8}\text{Sr}_{0.2}\text{NiO}_{4+\delta}$	600	2.17	[50]
		700	0.33	
$\text{BaCe}_{0.6}\text{Zr}_{0.2}\text{Y}_{0.2}\text{O}_{3-\delta}$ (BCZY2)	$\text{Pr}_2\text{NiO}_{4+\delta}$ -BCZY2	600	0.21	[51]
		700	0.06	
BCZY1	$(\text{Pr}_{0.9}\text{La}_{0.1})_2\text{Ni}_{0.74}\text{Cu}_{0.21}\text{Nb}_{0.05}\text{O}_{4+\delta}$ - BCZY1 (infiltration)	600	0.32	[52]
		700	0.13	
$\text{BaCe}_{0.9}\text{Y}_{0.1}\text{O}_{3-\delta}$	$\text{Pr}_2\text{NiO}_{4+\delta}$	600	0.80	[53]

¹ Polarization resistance of the Ni-cermets is assumed to be much lower than that of $\text{Pr}_2\text{NiO}_{4+\delta}$ -based electrodes.

3.5. Effect of Air and Hydrogen Humidification

It is well-known that water vapor partial pressure is a parameter determining proton transport in proton-conducting electrolyte membranes [54]. From the viewpoint of the bulk structure of such

membranes, humidification of both atmospheres is favorable, since it results in a decrease both of oxygen vacancies and hole concentrations:



and, correspondingly, improved proton transport. At the same time, air humidification is considered to be a more effective and easy way of suppressing some of the undesirable electronic conductivity of cerates and zirconates [55,56].

From the perspective of thermodynamic features, the maximal achievable electrical potential difference of a PCC (E or OCV) decreases with gas humidification, which follows from the corresponding decrease in partial pressure gradients [57,58]:

$$E = t_{i,\text{av}} \frac{RT}{4F} \ln\left(\frac{p'_{\text{O}_2}}{p''_{\text{O}_2}}\right) + t_{\text{H},\text{av}} \frac{RT}{2F} \ln\left(\frac{p''_{\text{H}_2\text{O}}}{p'_{\text{H}_2\text{O}}}\right) = t_{i,\text{av}} E_{\text{O}} + t_{\text{H},\text{av}} E_{\text{H}_2\text{O}}, \quad (8)$$

where p'_{O_2} and p''_{O_2} are the oxygen partial pressures in reducing and oxidizing atmospheres, $p'_{\text{H}_2\text{O}}$, $p''_{\text{H}_2\text{O}}$ are the water vapor partial pressures, E_{O} and $E_{\text{H}_2\text{O}}$ are the electrical potential differences of oxygen- and steam-concentration cells, $t_{\text{H},\text{av}}$ is the average proton transference number. Such a decrease negatively affects the performance of the cells operated in fuel cell mode because, in order to obtain high power densities, high OCVs are necessary [59]:

$$P_{\text{max}} = \frac{E^2}{4R_{\text{total}}}. \quad (9)$$

Conversely, the lowest possible OCVs are needed for cells operated in electrolysis cell mode if these OCVs are not associated with significant electron transport of the electrolytes or imperfect system gas-tightness. In detail, a current density will be higher at a certain voltage value (U), while a difference of $U-E$ will be higher (or E will be lower).

In order to check the $p_{\text{H}_2\text{O}}$ effect, both atmospheres were consequentially humidified: first, air atmosphere and then hydrogen atmosphere. Moreover, this allows the response of each electrode to be revealed and even their contributions to the total polarization resistance, R_p , to be estimated.

Figure 8 shows the main electrochemical characteristics of the PCC obtained under isothermal conditions with gradual increase of $p_{\text{H}_2\text{O}}$. As can be seen from these data, the OCVs drop from 0.979 to 0.899 V, the maximal power density decreases from 430 to 290 mW cm^{-2} , while the maximal achievable hydrogen flux density increases from 4.4 to 5.1 $\text{ml min}^{-1} \text{cm}^{-2}$, respectively, when $p''_{\text{H}_2\text{O}}$ increases from 0.03 to 0.5 atm. This is in complete agreement with the abovementioned thermodynamic predictions.

EIS and DRT analyses were further utilized to reveal the main tendencies in R_o and R_p changes and their effects on the PCC's performance.

Air humidification virtually does not change the spectra's shape (Figure A2); they, as well as the original spectra, can accurately be described by an equivalent circuit scheme with two RQ-elements. On the base of DRT data (Figure A3), the distribution function consists of three well-separated peaks at high $p''_{\text{H}_2\text{O}}$ values, two of which merge at lower $p''_{\text{H}_2\text{O}}$ values. The total polarization resistance of the electrodes amounts 0.07, 0.08, 0.10 and 0.12 Ωcm^2 at 0.03, 0.10, 0.30 and 0.50 atm of $p''_{\text{H}_2\text{O}}$. At the same time, the partial resistance components vary differently (Figure A4):

- (1) The absolute value of R_1 is equal to 0.02 Ωcm^2 , but its contribution as part of R_p decreases from 30 to 17%;
- (2) The contribution of R_1' in R_p does not exceed 4.5% or 0.004 Ωcm^2 in absolute units;
- (3) The contribution of R_2 increases from 70 to 80%, remaining the dominant parameter in the electrode performance.

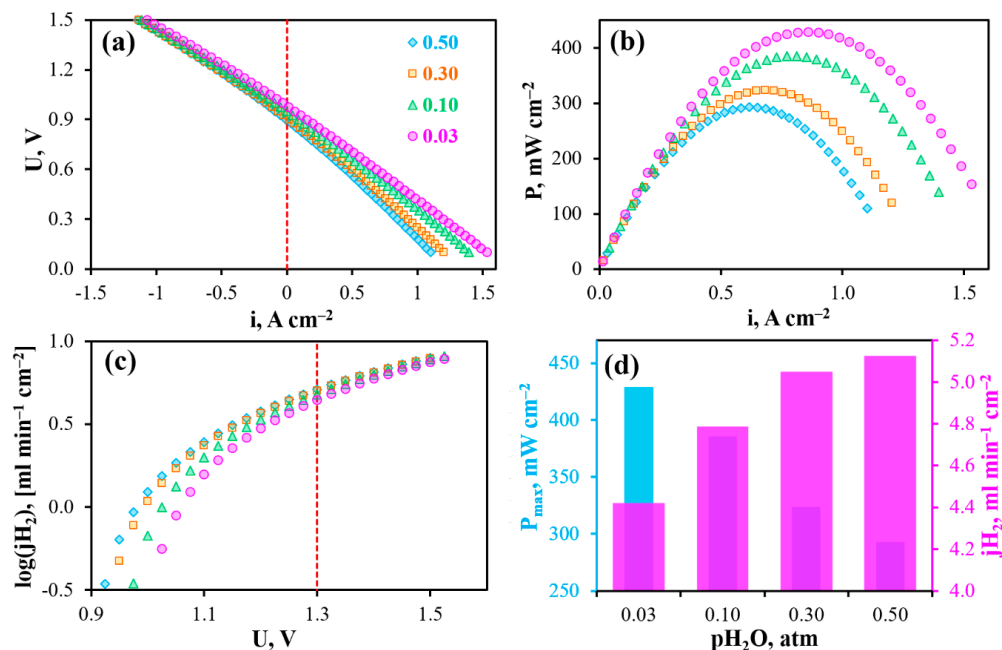


Figure 8. Reversible operation of the PCC at 750 °C depending on different $p_{\text{H}_2\text{O}}$ in wet air with the constant fuel gas composition (3% $\text{H}_2\text{O}/\text{H}_2$): volt-ampere curves (a), power density characteristics (b), maximal achievable hydrogen flux density (c), maximal power density and hydrogen flux density at $U = 1.3$ V depending on $p_{\text{H}_2\text{O}}$ (d).

All the mentioned components are sensitive towards air humidification. Therefore, these stages are primarily associated with oxygen electrode behavior.

Returning to the data of Figure 8, it can be stated that performance of the PCC is regulated by the electrode activity, which dominates under OCV and fuel cell modes of operation. When the bias exceeds the OCV level, the electrode resistance drops rapidly [60]; in this case, an improvement in PCC's performance is related with a lower R_0 as a result of achieving excellent proton conductivity in highly humid conditions. Making a preliminary conclusion, it can be noted that the $\text{Pr}_2\text{NiO}_{4+\delta}$ -based electrodes operate as a classical mixed oxygen-ionic/electronic conductor with no evidence of proton transportation revealed in previously published works [51,61]. However, this might be explained by the relatively high measured temperature (750 °C) leading to the insignificant water uptake capability of nickelates.

Finally, the PCC was tested depending on temperature under 50% $\text{H}_2\text{O}/\text{H}_2$ —50% $\text{H}_2\text{O}/\text{air}$ conditions, corresponding to both highly-moisturized gases (Figure 9). As listed in Table A1, further hydrogen humidification from 0.03 to 0.5 atm has little effect on both maximal power density (decreases by ~3%) and the hydrogen evolution rate (increases by ~6%). Therefore, differences in output parameters obtained at $p'_{\text{H}_2\text{O}} = p''_{\text{H}_2\text{O}} = 0.03$ atm (condition 1) and $p'_{\text{H}_2\text{O}} = p''_{\text{H}_2\text{O}} = 0.5$ atm (condition 2) are mainly attributed with the $p_{\text{H}_2\text{O}}$ variation in air atmosphere. Such differences amount to −37% of P_{max} and +13% of j_{H_2} at the same comparison temperature as shown in Figure 9d. The obtained data are also in agreement with thermodynamic predictions, in particular with OCVs, which reach 0.991, 0.951, 0.912 and 0.874 V at 600, 650, 700 and 750 °C, respectively.

With increasing $p_{\text{H}_2\text{O}}$ in hydrogen atmosphere, the impedance spectra cannot be described by the used equivalent circuit schemes, implying the appearance of additional rate-determining steps. These steps might be attributed either to fuel electrode processes or even to those taking place at the oxygen electrode. The latter is realized due to the fact that a change in a potential-determined parameter from the one side of an electrolyte membrane results in a redistribution of the overall potential and internal (ionic and electronic) currents, which can in turn affect the electrode process at the other side of the same membrane. As indicated in Figure A5, hydrogen humidification (when the

oxidizing composition is unchanged) leads to the formation of a new distribution function, consisting in different number of peaks, as well as their intensity and displacement. Such a distribution function becomes more complicated with decreasing temperature (Figure 10): here, at least five independent peaks and corresponding processes can be distinguished.

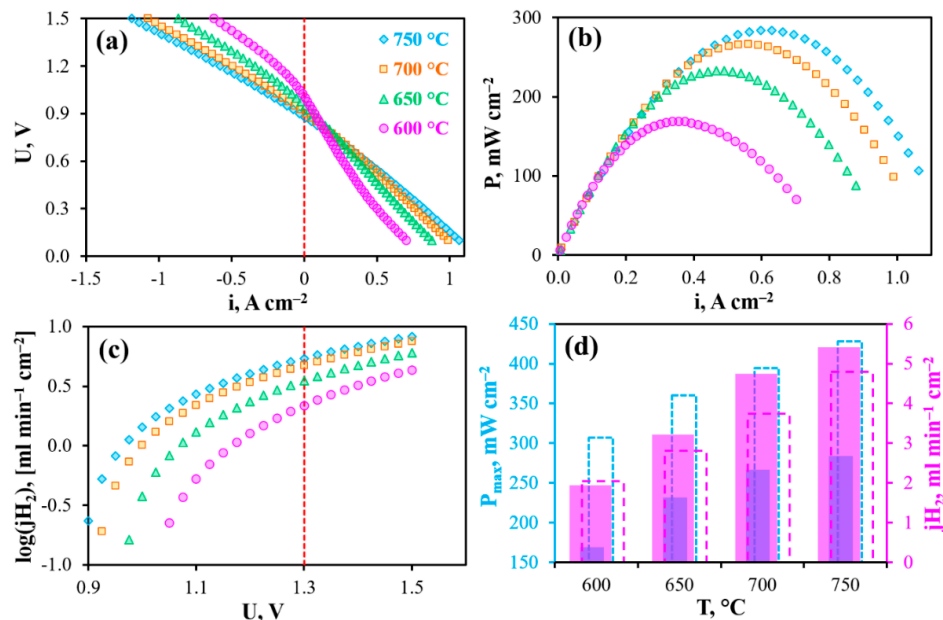


Figure 9. Reversible operation of the PCC at different temperatures under 50% $\text{H}_2\text{O}/\text{H}_2$ —50% $\text{H}_2\text{O}/\text{air}$ conditions: volt-ampere curves (a), power density characteristics (b), maximal achievable hydrogen flux density (c), maximal power density and hydrogen flux density at $U = 1.3$ V depending on temperature compared with those (dashed columns) obtained under 3% $\text{H}_2\text{O}/\text{H}_2$ —3% $\text{H}_2\text{O}/\text{air}$ conditions (d).

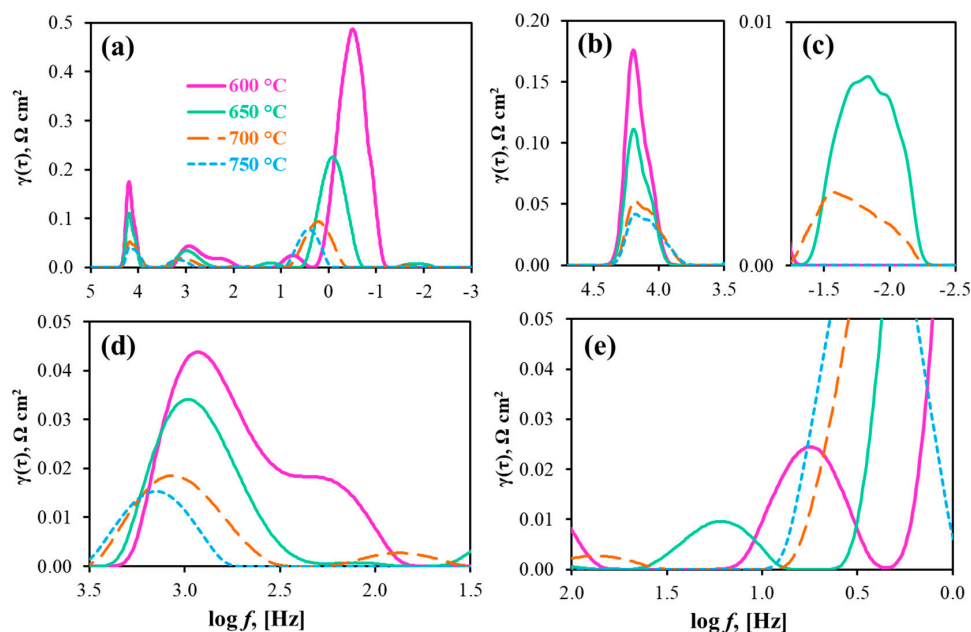


Figure 10. DRT results for the impedance spectra measured for the PCC at different temperatures under 50% $\text{H}_2\text{O}/\text{H}_2$ —50% $\text{H}_2\text{O}/\text{air}$ and OCV conditions: general view (a) and its parts at different magnifications (b–e).

Due to the already mentioned peculiarities, the R_0 values were determined as a high-frequency intercept of spectra with the x-axis, while the R_p values were separately estimated as the total area

bounded by a $\gamma(\tau)$ function. For 50% $\text{H}_2\text{O}/\text{H}_2$ —50% $\text{H}_2\text{O}/\text{air}$ and OCV conditions, R_O is equal to 0.51, 0.48, 0.45 and 0.42 $\Omega \text{ cm}^2$, whereas R_p is equal to 0.99, 0.46, 0.21 and 0.14 $\Omega \text{ cm}^2$ at 600, 650, 700 and 750 $^\circ\text{C}$, respectively. Comparing 50% $\text{H}_2\text{O}/\text{H}_2$ —50% $\text{H}_2\text{O}/\text{air}$ and 3% $\text{H}_2\text{O}/\text{H}_2$ —50% $\text{H}_2\text{O}/\text{air}$ conditions at 750 $^\circ\text{C}$, the R_O parameter is virtually unchanged, showing the possibility of full hydration of the proton-conducting electrolyte. At the same time, R_p increases from 0.12 to 0.14 $\Omega \text{ cm}^2$. Such an increment of R_p reaches 0.99 $\Omega \text{ cm}^2$ at 600 $^\circ\text{C}$ and 0.21 $\Omega \text{ cm}^2$ at 700 $^\circ\text{C}$ for 50% $\text{H}_2\text{O}/\text{H}_2$ —50% $\text{H}_2\text{O}/\text{air}$ conditions as against 0.39 $\Omega \text{ cm}^2$ at 600 $^\circ\text{C}$ and 0.12 $\Omega \text{ cm}^2$ at 700 $^\circ\text{C}$ for 3% $\text{H}_2\text{O}/\text{H}_2$ —3% $\text{H}_2\text{O}/\text{air}$ conditions. Therefore, not only air humidification, but also hydrogen moisturization leads to higher R_p values and correspondingly lower performance characteristics. It should be noted that neither R_O nor R_p indicates the efficiency of the PCC, which can, however, be estimated on the basis of the electrolytic domain boundaries (absolute level and contribution of ionic conductivity).

3.6. Electrolytic Properties of the BCZD Membrane

In order to estimate the electrolytic properties of BCZD, which determines rPCCs' efficiency [62–64], the $t_{i,av}$ values were calculated (Equation (1)) using data on R_O and R_p . According to Figure 11, the ionic transference numbers decrease naturally with increasing temperature due to an increase in the hole conductivity contribution. Nevertheless, the $t_{i,av}$ parameter achieves quite a high level (0.90 at 750 $^\circ\text{C}$) and, at the same time, can be further increased (up to 0.95 at the same temperature) via humidification of both gases. As a result of high saturation, oxygen vacancies are almost fully filled with steam, leading to a higher concentration of proton charge carriers (Equation (6)) and inhibition of hole charge carrier formation due to the lower concentration of free oxygen vacancies (Equation (7)).

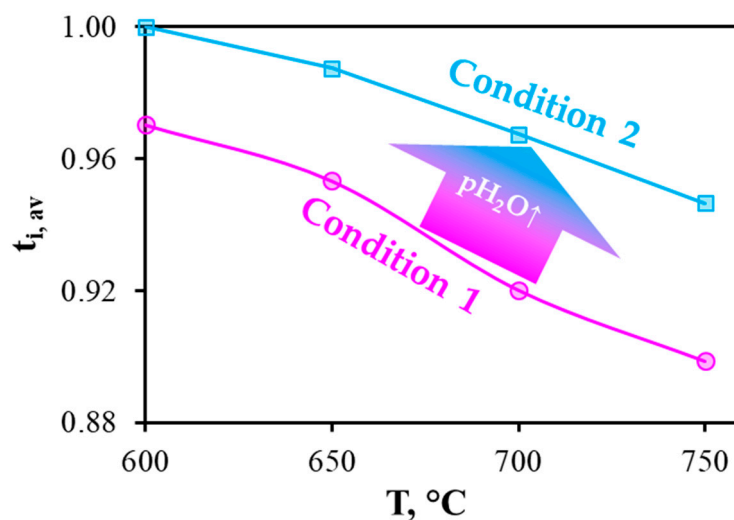


Figure 11. Temperature dependences of the average ionic transference numbers of the BCZD electrolyte membrane in the current-free mode of the rPCC under condition 1 ($p'\text{H}_2\text{O} = p''\text{H}_2\text{O} = 0.03 \text{ atm}$) and condition 2 ($p'\text{H}_2\text{O} = p''\text{H}_2\text{O} = 0.5 \text{ atm}$).

The average ionic conductivity of the electrolyte membranes, determined as

$$\sigma_{i,av} = \frac{h}{R_O} \cdot t_{i,av}, \quad (10)$$

should be considered as the most appropriate parameter (instead of total conductivity) related simultaneously with the performance (h/R_O) as well as the efficiency ($t_{i,av}$) of the electrochemical devices. For the present case, the average ionic conductivity of BCZD reaches 4.7 and 4.9 mS cm^{-1} at 600 and 700 $^\circ\text{C}$ under condition 1 and 4.9 and 5.4 mS cm^{-1} , respectively, under condition 2. These belong to a range of the highest values reached for proton-conducting electrolytes (Table 2, [37,52,65–79]),

which agrees with the independently measured comparison of ionic conductivities of Y- and Dy-doped Ba(Ce,Zr)O₃ [80]. The abovementioned results allow the following important conclusions to be formulated:

- (1) The BCZD electrolyte forms the basis for the design of novel electrochemical cells with improved output parameters due to its higher ionic conductivity compared with those for the most-studied Y-containing cerate-zirconates;
- (2) Despite the negative electrochemical response of the electrodes to gas humidification, the average ionic transference and ionic conductivity values take the opposite direction, resulting in improved PCC efficiency.

Table 2. Electrolytic properties of proton-conducting membranes of PCCs under OCV conditions ¹: h is the thickness, T is the temperature, E is the OCV, R_O and R_p are the ohmic and polarization resistances, t_{i,av} is the average ionic transference number, σ_{av} and σ_{i,av} are the average values of total and ionic conductivities of the electrolyte membranes.

Oxygen Electrode ²	Electrolyte ³	h, μm	T, °C	E, V	R _O , Ω cm ²	R _p , Ω cm ²	t _{i,av}	σ _{av} , mS cm ⁻¹	σ _{i,av} , mS cm ⁻¹	Ref.
PBN	BCZD	25	600	1.076	0.52	0.39	0.97	4.8	4.7	This work
SFM	BZCY8	1200	700	1.006	0.47	0.12	0.92	5.3	4.9	
SFM	BZCY8	20	600	1.03	0.80	1.47	0.97	2.5	2.4	[65]
			700	0.96	0.57	0.33	0.91	3.5	3.2	[66]
PLNCN	BCZY1	12	600	0.99	0.33	0.32	0.94	3.6	3.4	[52]
			700	0.95	0.21	0.13	0.91	5.8	5.2	
PBC	BCZYYC	10	600	1.00	0.37	0.34	0.94	2.7	2.5	[67]
			700	0.99	0.26	0.12	0.92	3.8	3.5	
SSC-BCZY1'	BCZY1'	9	600	1.13	0.47	0.42	1.00	1.9	1.9	[68]
			700	1.07	0.31	0.10	0.97	2.9	2.8	
GBSC	BCZY1	20	600	1.01	0.65	0.39	0.93	3.1	2.8	[69]
			700	1.02	0.52	0.08	0.92	3.8	3.6	
NBFN	BCZY1	40	600	1.11	0.84	0.71	0.99	4.8	4.7	[70]
	BCZY4	30	600	1.07	0.72	0.24	0.96	4.2	3.9	
			700	1.01	0.58	0.07	0.91	5.2	4.7	
	BCZY6	30	600	1.06	0.58	0.13	0.95	5.2	4.9	
LSCF			700	0.99	0.46	0.04	0.90	6.5	5.8	[37]
	BCZY7	30	600	1.04	1.37	0.65	0.94	2.2	2.1	
			700	0.96	0.97	0.21	0.88	3.1	2.7	
	BZY	30	600	0.93	1.34	0.82	0.89	2.2	1.9	
			700	0.84	1.13	0.29	0.80	2.7	2.1	
BSCF	BCZY1'	6	600	1.04	0.37	0.85	0.98	1.6	1.6	[71]
LSCF-BCZY3.5	BCZY3.5	8	600	1.05	0.31	1.25	0.99	2.6	2.6	[72]
			700	1.02	0.22	0.30	0.96	3.6	3.5	
LSCF-BSCZGY	BSCZGY	10	600	1.15	0.41	3.46	1.00	2.4	2.4	[73]
			700	1.13	0.19	1.82	1.00	5.4	5.4	
PBFM-SSC	BCZY1	25	600	1.01	0.41	0.54	0.95	6.1	5.8	[74]
NBFC	BCZD	30	600	1.05	0.68	0.66	0.96	4.4	4.2	[75]
			700	1.01	0.42	0.24	0.94	7.1	6.7	
NBFC'	BCZYY	25	600	1.04	1.04	0.83	0.95	2.4	2.3	[76]
			700	1.01	0.65	0.22	0.92	3.8	3.6	
PBC-BCZY	BCZY0.3	17	600	1.01	0.32	0.64	0.96	5.3	5.1	[77]
BFCC	BCZYY'	30	600	1.06	0.49	0.28	0.96	6.1	5.9	[78]
YBCZ	BCZD	20	600	1.03	0.77	0.51	0.94	2.6	2.5	[79]
			700	0.95	0.49	0.18	0.89	4.4	3.6	

¹ In the most cases for the listed PCCs, the gas compositions represent wet (3%H₂O) H₂ and static (or wet) air. ² Abbreviations of oxygen electrodes: PBN = Pr_{1.9}Ba_{0.1}NiO_{4+δ}, SFM = SrFe_{0.75}Mo_{0.25}O_{3-δ}, PLNCN = (Pr_{0.9}La_{0.1})₂Ni_{0.74}Cu_{0.21}Nb_{0.05}O_{4+δ}, PBC = PrBaCo₂O_{5+δ}, SSC = Sm_{0.5}Sr_{0.5}CoO_{3-δ}, GBSC = GdBa_{0.5}Sr_{0.5}Co₂O_{5+δ}, NBFN = Nd_{0.5}Ba_{0.5}Fe_{0.9}Ni_{0.1}O_{3-δ}, LSCF = La_{0.6}Sr_{0.4}Co_{0.2}Fe_{0.8}O_{3-δ}, BSCF = Ba_{0.5}Sr_{0.5}Co_{0.8}Fe_{0.2}O_{3-δ}, PBFM = (PrBa)_{0.95}(Fe_{0.9}Mo_{0.1})₂O_{5-δ}, NBFC = Nd_{0.5}Ba_{0.5}Fe_{0.9}Co_{0.1}O_{3-δ}, NBFC' = Nd_{0.5}Ba_{0.5}Fe_{0.9}Cu_{0.1}O_{3-δ}, PBC = PrBaCo₂O_{5+δ}, BFCC = BaFe_{0.6}Co_{0.3}Ce_{0.1}O_{3-δ}, YBCZ = YBaCo_{3.5}Zn_{0.5}O_{7+δ}. ³ Abbreviations of electrolytes: BCZD = BaCe_{0.5}Zr_{0.3}Dy_{0.2}O_{3-δ}, BCZY1 = BaCe_{0.7}Zr_{0.1}Y_{0.2}O_{3-δ}, BCZY1' = BaCe_{0.8}Zr_{0.1}Y_{0.1}O_{3-δ}, BCZY3 = BaCe_{0.5}Zr_{0.3}Y_{0.2}O_{3-δ}, BCZY3.5 = BaCe_{0.5}Zr_{0.35}Y_{0.15}O_{3-δ}, BCZY4 = BaZr_{0.4}Ce_{0.4}Y_{0.2}O_{3-δ}, BCZY6 = BaZr_{0.6}Ce_{0.2}Y_{0.2}O_{3-δ}, BCZY7 = BaZr_{0.7}Ce_{0.1}Y_{0.2}O_{3-δ}, BZCY8 = BaCe_{0.1}Zr_{0.8}Y_{0.1}O_{3-δ}, BZY = BaZr_{0.8}Y_{0.2}O_{3-δ}, BSCZGY = Ba_{0.5}Sr_{0.5}Ce_{0.6}Zr_{0.2}Gd_{0.1}Y_{0.1}O_{3-δ}, BCZYY = BaCe_{0.5}Zr_{0.3}Y_{0.1}Yb_{0.1}O_{3-δ}, BCZYY' = BaCe_{0.7}Zr_{0.1}Y_{0.1}Yb_{0.1}O_{3-δ}, BCZYYC = BaCe_{0.68}Zr_{0.1}Y_{0.1}Yb_{0.1}Co_{0.02}O_{3-δ}.

4. Conclusions

This work presents the results of fabrication and characterization of a reversible protonic ceramic cell having symmetrically-organized electrodes made of $\text{Pr}_{1.9}\text{Ba}_{0.1}\text{NiO}_{4+\delta}$ (PBN). Utilization of the same material as the functional fuel and oxygen electrode allows minimization of the thermo-chemical stress between the functional materials during high-temperature steps and even a reduction of these steps to one sintering stage, promising significant techno-economic benefits. The fabricated cell based on a 25 μm -thick $\text{BaCe}_{0.5}\text{Zr}_{0.3}\text{Dy}_{0.2}\text{O}_{3-\delta}$ (BCZD) proton-conducting electrolyte demonstrated output characteristics as high as $\sim 300 \text{ mW cm}^{-2}$ at 600 $^{\circ}\text{C}$ in fuel cell mode and $\sim 300 \text{ mA cm}^{-2}$ in electrolysis cell mode at thermoneutral conditions. The cell was tested under conditions of varying humidity in order to evaluate electrode and electrolyte performance. It was found that the PBN–BCZD oxygen electrode determined the overall electrode performance at 750 $^{\circ}\text{C}$, operating as a dual conducting ($\text{O}^{2-}/\text{h}^{\bullet}$) system due to the negative electrochemical response to gas humidification. As a consequence of the high contribution of polarization resistance to the total resistance, the response of the rPCC's performance was the same under open circuit voltage and fuel cell modes. On the other hand, the ohmic resistance and the average ionic transference numbers of the electrolyte membrane increased with increasing humidification, demonstrating its proton-conducting nature. Along with increased efficiency (as a result of improved electrolytic properties), the performance of the PCC was higher under humidification due to the total cell resistance being determined by the ohmic component. Although only medium performance was reached in this work (due to the rather thick electrolyte, 25 μm), the proposed strategies can effectively be used in future to resolve a number of technological issues.

Author Contributions: Conceptualization, D.M.; Methodology, J.L. and G.V.; Validation, A.D.; Formal analysis, A.F. and S.P.; Investigation, A.T., J.L. and G.V.; Resources, A.T. and J.L.; Writing—original draft preparation, D.M.; Writing—review & editing, D.M.; Visualization, A.T.; Supervision, A.D.; Project administration, D.M.; Funding acquisition, D.M.

Funding: The majority of this work was carried out under the budgetary plans of Institute of High Temperature Electrochemistry. The design of new electrode materials and their characterization was also funded by the Russian Foundation for Basic Research, grant number 18-38-20063. Dr. Dmitry Medvedev is also grateful to the Council of the President of the Russian Federation (scholarship CII-161.2018.1) for supporting the studies devoted to search of new Co-free electrode materials.

Acknowledgments: The characterization of powder and ceramic materials was carried out at the Shared Access Centre “Composition of Compounds” of the Institute of High Temperature Electrochemistry [26].

Conflicts of Interest: The authors declare no conflict of interest.

Appendix A

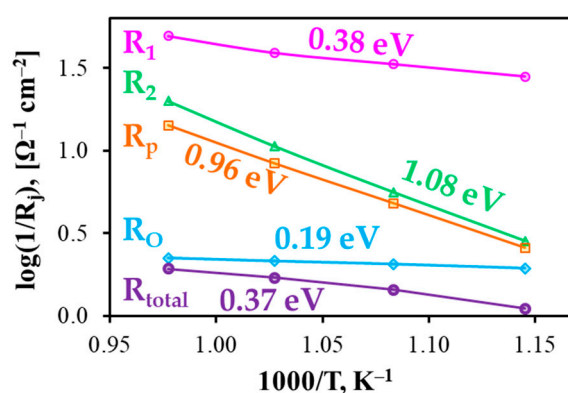


Figure A1. Temperature dependences of constitute resistances (R_j) of the fabricated PCC in Arrhenius coordinates. The corresponding activation energies calculated in Frenkel coordinates ($\log(T/R_j) = f(1/T)$) are also presented.

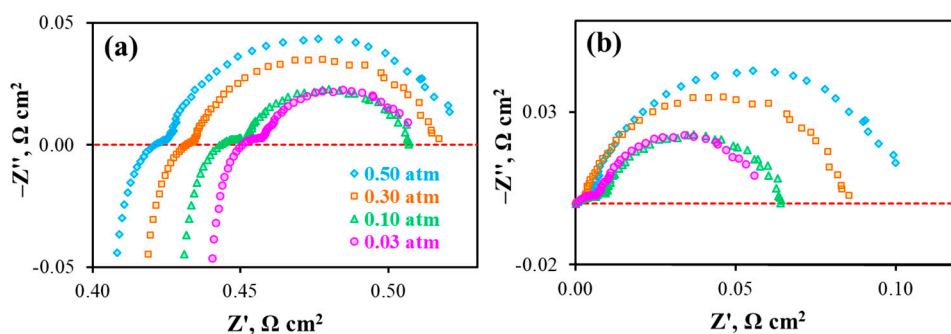


Figure A2. Impedance spectra of the PCC at 750 °C and OCV conditions depending on different p_{H_2O} in air atmosphere (fuel gas is 3% H_2O/H_2): original spectra (a) and those obtained after subtracting the ohmic resistance (b).

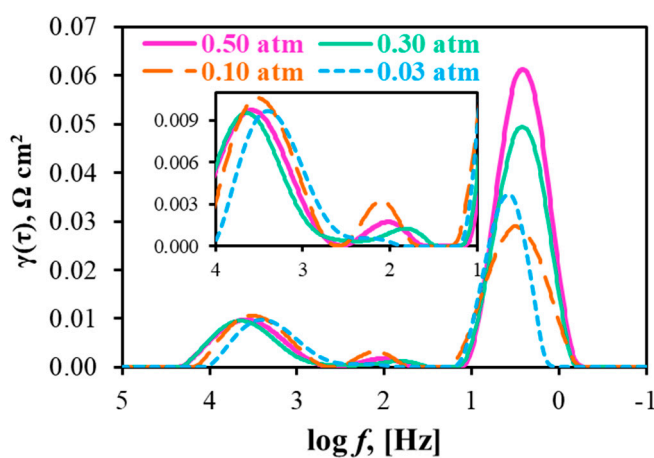


Figure A3. DRT results for the impedance spectra presented in Figure A2.

Table A1. Effect of hydrogen humidification on the PCC performance at 700 °C, when $p_{H_2O} = 0.50$ atm. R_O and R_p are presented for OCV mode, while j_{H_2} is presented at $U = 1.3$ V.

p_{H_2O} , atm	R_O , $\Omega\text{ cm}^2$	R_p , $\Omega\text{ cm}^2$	P_{max} , mW cm^{-2}	j_{H_2} , $\text{ml min}^{-1}\text{ cm}^{-2}$
0.03	0.47	0.12	293	5.1
0.50	0.45	0.21	284	5.6

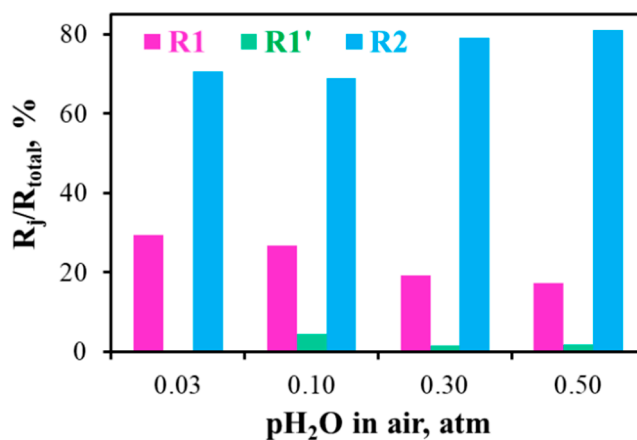


Figure A4. Contribution of partial resistances in the total resistance of the electrodes (R_p). These data were obtained from the DRT results (Figure A3).

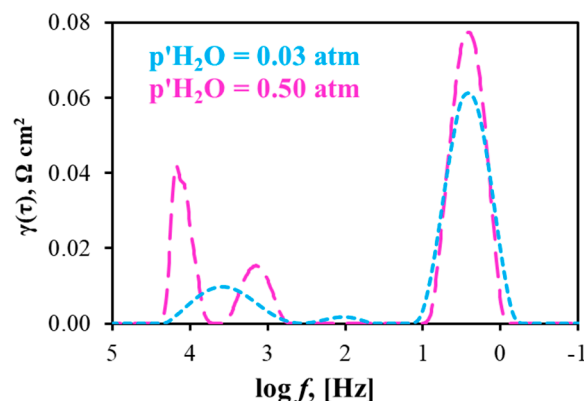


Figure A5. DRT results for the impedance spectra measured for the PCC at 750 °C under OCV conditions at different $p''\text{H}_2\text{O}$ values in hydrogen atmosphere ($p''\text{H}_2\text{O}$ in air is equal 0.5 atm).

References

1. Medvedev, D.; Murashkina, A.; Pikalova, E.; Demin, A.; Podias, A.; Tsiakaras, P. BaCeO₃: Materials development, properties and application. *Prog. Mater. Sci.* **2014**, *60*, 72–129. [[CrossRef](#)]
2. Bi, L.; Boulfrada, S.; Traversa, E. Steam electrolysis by solid oxide electrolysis cells (SOECs) with proton-conducting oxides. *Chem. Soc. Rev.* **2014**, *43*, 8255–8270. [[CrossRef](#)] [[PubMed](#)]
3. Choi, S.M.; An, H.; Yoon, K.J.; Kim, B.-K.; Lee, H.-W.; Son, J.-W.; Kim, H.; Shin, D.; Ji, H.-L. Electrochemical analysis of high-performance protonic ceramic fuel cells based on a columnar-structured thin electrolyte. *Appl. Energy* **2019**, *233–234*, 29–36. [[CrossRef](#)]
4. Mohato, N.; Banerjee, A.; Gupta, A.; Omar, S.; Balani, K. Progress in material selection for solid oxide fuel cell technology: A review. *Prog. Mater. Sci.* **2015**, *72*, 141–337. [[CrossRef](#)]
5. Gómez, S.Y.; Hotza, D. Current developments in reversible solid oxide fuel cells. *Renew. Sust. Energy Rev.* **2016**, *61*, 155–174. [[CrossRef](#)]
6. Choi, S.; Kucharczyk, C.J.; Liang, Y.; Zhang, X.; Takeuchi, I.; Ji, H.-I.; Haile, S.M. Exceptional power density and stability at intermediate temperatures in protonic ceramic fuel cells. *Nat. Energy* **2018**, *3*, 202–210. [[CrossRef](#)]
7. Bae, K.; Jang, D.Y.; Choi, H.J.; Kim, D.; Hong, J.; Kim, B.-K.; Lee, J.-H.; Son, J.-W.; Shim, J.H. Demonstrating the potential of yttrium-doped barium zirconate electrolyte for high-performance fuel cells. *Nat. Commun.* **2017**, *8*, 14553. [[CrossRef](#)] [[PubMed](#)]
8. Duan, C.; Tong, J.; Shang, M.; Nikodemski, S.; Sanders, M.; Ricote, S.; Almansoori, A.; O'Hayre, R. Readily processed protonic ceramic fuel cells with high performance at low temperatures. *Science* **2015**, *349*, 1321–1326. [[CrossRef](#)]
9. Shim, J.H. Ceramics breakthrough. *Nat. Energy* **2018**, *3*, 168–169. [[CrossRef](#)]
10. Ding, D.; Li, X.; Lai, S.Y.; Gerdes, K.; Liu, M. Enhancing SOFC cathode performance by surface modification through infiltration. *Energy Environ. Sci.* **2014**, *7*, 552–575. [[CrossRef](#)]
11. Zheng, Y.; Wang, J.; Yu, B.; Zhang, W.; Chen, J.; Qiao, J.; Zhang, J. A review of high temperature co-electrolysis of H₂O and CO₂ to produce sustainable fuels using solid oxide electrolysis cells (SOECs): Advanced materials and technology. *Chem. Soc. Rev.* **2017**, *46*, 1427–1463. [[CrossRef](#)] [[PubMed](#)]
12. Su, C.; Wang, W.; Liu, M.; Tadé, M.O.; Shao, Z. Progress and prospects in symmetrical solid oxide fuel cells with two identical electrodes. *Adv. Energy Mater.* **2015**, *5*, 1500188. [[CrossRef](#)]
13. Choi, S.; Sengodan, S.; Park, S.; Ju, Y.-W.; Kim, J.; Hyodo, J.; Jeong, H.Y.; Ishihara, T.; Shin, J.; Kim, G. A robust symmetrical electrode with layered perovskite structure for direct hydrocarbon solid oxide fuel cells: PrBa_{0.8}Ca_{0.2}Mn₂O_{5+δ}. *J. Mater. Chem. A* **2016**, *4*, 1747–1753. [[CrossRef](#)]
14. Shen, J.; Chen, Y.; Yang, G.; Zhou, W.; Tadé, M.O.; Shao, Z. Impregnated LaCo_{0.3}Fe_{0.67}Pd_{0.03}O_{3-δ} as a promising electrocatalyst for “symmetrical” intermediate-temperature solid oxide fuel cells. *J. Power Sources* **2016**, *306*, 92–99. [[CrossRef](#)]
15. Tao, H.; Xie, J.; Wu, Y.; Wang, S. Evaluation of PrNi_{0.4}Fe_{0.6}O_{3-δ} as a symmetrical SOFC electrode material. *Int. J. Hydrogen Energy* **2018**, *43*, 15423–15432. [[CrossRef](#)]

16. Niu, B.; Jin, F.; Zhang, L.; Shen, P.; He, T. Performance of double perovskite symmetrical electrode materials $\text{Sr}_2\text{TiFe}_{1-x}\text{Mo}_x\text{O}_{6-\delta}$ ($x = 0.1, 0.2$) for solid oxide fuel cells. *Electrochim. Acta* **2018**, *263*, 217–227. [CrossRef]
17. Lan, R.; Cowin, P.I.; Sengodan, S.; Tao, S. A perovskite oxide with high conductivities in both air and reducing atmosphere for use as electrode for solid oxide fuel cells. *Sci. Rep.* **2016**, *6*. [CrossRef]
18. Gao, Z.; Ding, X.; Ding, D.; Ding, L.; Zhang, S.; Yuan, G. Infiltrated Pr_2NiO_4 as promising bi-electrode for symmetrical solid oxide fuel cells. *Int. J. Hydrogen Energy* **2018**, *43*, 8953–8961. [CrossRef]
19. Nicollet, C.; Flura, A.; Vibhu, V.; Rougier, A.; Bassat, J.-M.; Grenier, J.-C. An innovative efficient oxygen electrode for SOFC: Pr_6O_{11} infiltrated into Gd-doped ceria backbone. *Int. J. Hydrogen Energy* **2016**, *41*, 15538–15544. [CrossRef]
20. Lyagaeva, J.; Medvedev, D.; Pikalova, E.; Plaksin, S.; Brouzgou, A.; Demin, A.; Tsiakaras, P. A detailed analysis of thermal and chemical compatibility of cathode materials suitable for $\text{BaCe}_{0.8}\text{Y}_{0.2}\text{O}_{3-\delta}$ and $\text{BaZr}_{0.8}\text{Y}_{0.2}\text{O}_{3-\delta}$ proton electrolytes for solid oxide fuel cell application. *Int. J. Hydrogen Energy* **2017**, *42*, 1715–1723. [CrossRef]
21. Pikalova, E.; Kolchugin, A.; Bogdanovich, N.; Medvedev, D.; Lyagaeva, J.; Vedmid', L.; Anayev, M.; Plaksin, S.; Farlenkov, A. Suitability of $\text{Pr}_{2-x}\text{Ca}_x\text{NiO}_{4+\delta}$ as cathode materials for electrochemical devices based on oxygen ion and proton conducting solid state electrolytes. *Int. J. Hydrogen Energy* **2018**. [CrossRef]
22. Sun, W.; Wang, Y.; Fang, S.; Zhu, Z.; Yan, L.; Liu, W. Evaluation of $\text{BaZr}_{0.1}\text{Ce}_{0.7}\text{Y}_{0.2}\text{O}_{3-\delta}$ -based proton-conducting solid oxide fuel cells fabricated by a one-step co-firing process. *Electrochim. Acta* **2011**, *56*, 1447–1454. [CrossRef]
23. Dai, H.; Da'as, E.H.; Shafi, S.P.; Wang, H.; Bi, L. Tailoring cathode composite boosts the performance of proton-conducting SOFCs fabricated by a one-step co-firing method. *J. Eur. Ceram. Soc.* **2018**, *38*, 2903–2908. [CrossRef]
24. Lyagaeva, J.; Danilov, N.; Vdovin, G.; Bu, J.; Medvedev, D.; Demin, A.; Tsiakaras, P. A new Dy-doped BaCeO_3 - BaZrO_3 proton-conducting material as a promising electrolyte for reversible solid oxide fuel cells. *J. Mater. Chem. A* **2016**, *4*, 15390–15399. [CrossRef]
25. Lyagaeva, Y.G.; Danilov, N.A.; Gorshkov, M.Y.; Vdovin, G.K.; Antonov, B.D.; Demin, A.K.; Medvedev, D.A. Functionality of lanthanum, neodymium, and praseodymium nickelates as promising electrode systems for proton-conducting electrolytes. *Russ. J. Appl. Chem* **2018**, *91*, 583–590. [CrossRef]
26. Equipment. Shared Access Center. Available online: http://www.ihte.uran.ru/?page_id=3154 (accessed on 11 December 2018).
27. DRTTOOLS. Available online: <https://sites.google.com/site/drttools/> (accessed on 11 December 2018).
28. Pikalova, E.; Kolchugin, A.; Filonova, E.; Bogdanovich, N.; Pikalov, S.; Ananyev, M.; Molchanova, N.; Farlenkov, A. Validation of calcium-doped neodymium nickelates as SOFC air electrode materials. *Solid State Ionics* **2018**, *319*, 130–140. [CrossRef]
29. Akbari-Fakhrabadi, A.; Toledo, E.G.; Canales, J.I.; Meruane, V.; Chan, S.H.; Gracia-Pinilla, M.A. Effect of Sr^{2+} and Ba^{2+} doping on structural stability and mechanical properties of $\text{La}_2\text{NiO}_{4+\delta}$. *Ceram. Int.* **2018**, *44*, 10551–10557. [CrossRef]
30. Kravchenko, E.; Khalyavin, D.; Zakharchuk, K.; Grins, J.; Svensson, G.; Pankov, V.; Yaremchenko, A. High-temperature characterization of oxygen-deficient K_2NiF_4 -type $\text{Nd}_{2-x}\text{Sr}_x\text{NiO}_{4-\delta}$ ($x = 1.0$ – 1.6) for potential SOFC/SOEC applications. *J. Mater. Chem. A* **2015**, *3*, 23852–23863. [CrossRef]
31. Hua, B.; Li, M.; Sun, Y.-F.; Li, J.-H.; Luo, J.-L. Enhancing perovskite electrocatalysis of solid oxide cells through controlled exsolution of nanoparticles. *ChemSusChem* **2017**, *10*, 3333–3341. [CrossRef]
32. Pikalova, E.Y.; Medvedev, D.A.; Khasanov, A.F. Structure, stability, and thermomechanical properties of Ca-substituted $\text{Pr}_2\text{NiO}_{4+\delta}$. *Phys. Solid State* **2017**, *59*, 694–702. [CrossRef]
33. Ceretti, M.; Wahyudi, O.; André, G.; Meven, M.; Villesuzanne, A.; Paulus, W. $(\text{Nd}/\text{Pr})_2\text{NiO}_{4+\delta}$: Reaction intermediates and redox behavior explored by in situ neutron powder diffraction during electrochemical oxygen intercalation. *Chem. Mater.* **2018**, *57*, 4657–4666. [CrossRef] [PubMed]
34. Løken, A.; Ricote, S.; Wachowski, S. Thermal and chemical expansion in proton ceramic electrolytes and compatible electrodes. *Crystals* **2018**, *8*, 365. [CrossRef]
35. Kharton, V.V.; Kovalevsky, A.V.; Avdeev, M.; Tsipis, E.V.; Patrakeevev, M.V.; Yaremchenko, A.A.; Naumovich, E.N.; Frade, J.R. Chemically induced expansion of $\text{La}_2\text{NiO}_{4+\delta}$ -based materials. *Chem. Mater.* **2007**, *19*, 2027–2033. [CrossRef]

36. Kochetova, N.; Animitsa, I.; Medvedev, D.; Demin, A.; Tsiakaras, P. Recent activity in the development of proton-conducting oxides for high-temperature applications. *RSC Adv.* **2016**, *6*, 73222–73268. [[CrossRef](#)]
37. Jeong, S.; Kobayashi, T.; Kuroda, K.; Kwon, H.; Zhu, C.; Habazaki, H.; Aoki, Y. Evaluation of thin film fuel cells with Zr-rich $\text{BaZr}_x\text{Ce}_{0.8-x}\text{Y}_{0.2}\text{O}_{3-\delta}$ electrolytes ($x \geq 0.4$) fabricated by a single-step reactive sintering method. *RSC Adv.* **2018**, *8*, 26309–26317. [[CrossRef](#)]
38. Danilov, N.A.; Lyagaeva, J.G.; Medvedev, D.A.; Demin, A.K.; Tsiakaras, P. Transport properties of highly dense proton-conducting $\text{BaCe}_{0.8-x}\text{Zr}_x\text{Dy}_{0.2}\text{O}_{3-\delta}$ materials in low- and high-temperature ranges. *Electrochim. Acta* **2018**, *284*, 551–559. [[CrossRef](#)]
39. Liu, M.; Hu, H. Effect of interfacial resistance on determination of transport properties of mixed-conducting electrolytes. *J. Electrochem. Soc.* **1996**, *143*, L109–L112. [[CrossRef](#)]
40. Kreuer, K.D. Proton-conducting oxides. *Annu. Rev. Mater. Res.* **2003**, *33*, 333–359. [[CrossRef](#)]
41. Malavasi, L.; Fisher, C.A.J.; Islam, M.S. Oxide-ion and proton conducting electrolyte materials for clean energy applications: Structural and mechanistic features. *Chem. Soc. Rev.* **2010**, *39*, 4370–4387. [[CrossRef](#)]
42. Gregori, G.; Merkle, R.; Maier, J. Ion conduction and redistribution at grain boundaries in oxide systems. *Prog. Mater. Sci.* **2017**, *89*, 252–305. [[CrossRef](#)]
43. Nechache, A.; Cassir, M.; Ringuedé, A. Solid oxide electrolysis cell analysis by means of electrochemical impedance spectroscopy: A review. *J. Power Sources* **2014**, *258*, 164–181. [[CrossRef](#)]
44. Zheng, M.; Wang, S.; Yang, Y.; Xia, C. Barium carbonate as a synergistic catalyst for the $\text{H}_2\text{O}/\text{CO}_2$ reduction reaction at Ni–yttria stabilized zirconia cathodes for solid oxide electrolysis cells. *J. Mater. Chem. A* **2018**, *6*, 2721–2729. [[CrossRef](#)]
45. Sun, S.; Cheng, Z. Electrochemical behaviors for Ag, LSCF and BSCF as oxygen electrodes for proton conducting IT-SOFC. *J. Electrochem. Soc.* **2017**, *164*, F3104–F3113. [[CrossRef](#)]
46. Shi, N.; Su, F.; Huan, D.; Xie, Y.; Lin, J.; Tan, W.; Peng, R.; Xia, C.; Chen, C.; Lu, Y. Performance and DRT analysis of P-SOFCs fabricated using new phase inversion combined tape casting technology. *J. Mater. Chem. A* **2017**, *5*, 19664–19671. [[CrossRef](#)]
47. Wang, X.; Ma, Z.; Zhang, T.; Kang, J.; Ou, X.; Feng, P.; Wang, S.; Zhou, F.; Ling, Y. Charge transfer modeling and polarization DRT analysis of proton ceramics fuel cells based on mixed conductive electrolyte with the modified anode-electrolyte interface. *ACS Appl. Mater. Interfaces* **2018**, *10*, 35047–35059. [[CrossRef](#)] [[PubMed](#)]
48. Boukamp, B.A. Fourier transform distribution function of relaxation times; application and limitations. *Electrochim. Acta* **2015**, *154*, 35–46. [[CrossRef](#)]
49. Ivers-Tiffée, E.; Weber, A. Evaluation of electrochemical impedance spectra by the distribution of relaxation times. *J. Ceram. Soc. Jpn.* **2017**, *125*, 193–201. [[CrossRef](#)]
50. Yang, S.; Wen, Y.; Zhang, J.; Lu, Y.; Ye, X.; Wen, Z. Electrochemical performance and stability of cobalt-free $\text{Ln}_{1.2}\text{Sr}_{0.8}\text{NiO}_4$ ($\text{Ln}=\text{La}$ and Pr) air electrodes for proton-conducting reversible solid oxide cells. *Electrochim. Acta* **2018**, *267*, 269–277. [[CrossRef](#)]
51. Li, W.; Guan, B.; Ma, L.; Hu, S.; Zhang, N.; Liu, X. High performing triple-conductive $\text{Pr}_2\text{NiO}_{4+\delta}$ anode for proton-conducting steam solid oxide electrolysis cell. *J. Mater. Chem. A* **2018**, *6*, 18057–18066. [[CrossRef](#)]
52. Li, G.; Jin, H.; Cui, Y.; Gui, L.; He, B.; Zhao, L. Application of a novel $(\text{Pr}_{0.9}\text{La}_{0.1})_2(\text{Ni}_{0.74}\text{Cu}_{0.21}\text{Nb}_{0.05})\text{O}_{4+\delta}$ -infiltrated $\text{BaZr}_{0.1}\text{Ce}_{0.7}\text{Y}_{0.2}\text{O}_{3-\delta}$ cathode for high performance protonic ceramic fuel cells. *J. Power Sources* **2017**, *341*, 192–198. [[CrossRef](#)]
53. Dailly, J.; Marrony, M.; Taillades, G.; Taillades-Jacquín, M.; Grimaud, A.; Mauvy, F.; Louradour, E.; Salmi, J. Evaluation of proton conducting BCY10-based anode supported cells by co-pressing method: Up-scaling, performances and durability. *J. Power Sources* **2014**, *255*, 302–307. [[CrossRef](#)]
54. Wang, W.; Medvedev, D.; Shao, Z. Gas Humidification impact on the properties and performance of perovskite-type functional materials in proton-conducting solid oxide cells. *Adv. Funct. Mater.* **2018**, *28*, 1802592. [[CrossRef](#)]
55. Heras-Juaristi, G.; Pérez-Coll, D.; Mather, G.C. Temperature dependence of partial conductivities of the $\text{BaZr}_{0.7}\text{Ce}_{0.2}\text{Y}_{0.1}\text{O}_{3-\delta}$ proton conductor. *J. Power Sources* **2017**, *364*, 52–60. [[CrossRef](#)]
56. Lyagaeva, J.; Danilov, N.; Korona, D.; Farlenkov, A.; Medvedev, D.; Demin, A.; Animitsa, I.; Tsiakaras, P. Improved ceramic and electrical properties of CaZrO_3 -based proton-conducting materials prepared by a new convenient combustion synthesis method. *Ceram. Int.* **2017**, *43*, 7184–7192. [[CrossRef](#)]
57. Norby, T. EMF method determination of conductivity contributions from protons and other foreign ions in oxides. *Solid State Ionics* **1988**, *28–30*, 1586–1591. [[CrossRef](#)]

58. Sutija, D. Transport number determination by the concentration-cell/open-circuit voltage method for oxides with mixed electronic, ionic and protonic conductivity. *Solid State Ionics* **1995**, *77*, 167–174. [[CrossRef](#)]
59. Gong, Z.; Sun, W.; Cao, J.; Shan, D.; Wu, Y.; Liu, W. Ce_{0.8}Sm_{0.2}O_{1.9} decorated with electron-blocking acceptor-doped BaCeO₃ as electrolyte for low-temperature solid oxide fuel cells. *Electrochim. Acta* **2017**, *228*, 226–232. [[CrossRef](#)]
60. Huan, D.; Shi, N.; Zhang, L.; Tan, W.; Xie, Y.; Wang, W.; Xia, C.; Lu, Y. New, Efficient, and reliable air electrode material for proton-conducting reversible solid oxide cells. *ACS Appl. Mater. Interfaces* **2018**, *10*, 1761–1770. [[CrossRef](#)]
61. Philippeau, B.; Mauvy, F.; Mazataud, C.; Fourcade, S.; Grenier, J.-C. Comparative study of electrochemical properties of mixed conducting Ln₂NiO_{4+δ} (Ln = La, Pr and Nd) and La_{0.6}Sr_{0.4}Fe_{0.8}Co_{0.2}O_{3-δ} as SOFC cathodes associated to Ce_{0.9}Gd_{0.1}O_{2-δ}, La_{0.8}Sr_{0.2}Ga_{0.8}Mg_{0.2}O_{3-δ} and La₉Sr₁Si₆O_{26.5} electrolytes. *Solid State Ionics* **2013**, *249–250*, 17–25. [[CrossRef](#)]
62. Nakamura, T.; Mizunuma, S.; Kimura, Y.; Mikami, Y.; Yamauchi, K.; Kuroha, T.; Taniguchi, N.; Tsuji, Y.; Okuyama, Y.; Amezawa, K. Energy efficiency of ionic transport through proton conducting ceramic electrolytes for energy conversion applications. *J. Mater. Chem. A* **2018**, *6*, 15771–15780. [[CrossRef](#)]
63. Ji, H.-I.; Kim, H.; Lee, H.-W.; Kim, B.-K.; Son, J.-W.; Yoon, K.J.; Lee, J.-H. Open-cell voltage and electrical conductivity of a protonic ceramic electrolyte under two chemical potential gradients. *Phys. Chem. Chem. Phys.* **2018**, *20*, 14997–15001. [[CrossRef](#)] [[PubMed](#)]
64. Zhang, J.-H.; Lei, L.-B.; Liu, D.; Zhao, F.-Y.; Ni, M.; Chen, F. Mathematical modeling of a proton-conducting solid oxide fuel cell with current leakage. *J. Power Sources* **2018**, *400*, 333–340. [[CrossRef](#)]
65. Wachowski, S.; Li, Z.; Polfus, J.M.; Norby, T. Performance and stability in H₂S of SrFe_{0.75}Mo_{0.25}O_{3-δ} as electrode in proton ceramic fuel cells. *J. Eur. Ceram. Soc.* **2018**, *38*, 163–171. [[CrossRef](#)]
66. Nasani, N.; Ramasamy, D.; Mikhalev, S.; Kovalevsky, A.V.; Fagg, D.P. Fabrication and electrochemical performance of a stable, anode supported thin BaCe_{0.4}Zr_{0.4}Y_{0.2}O_{3-δ} electrolyte protonic ceramic fuel cell. *J. Power Sources* **2015**, *278*, 582–589. [[CrossRef](#)]
67. Wan, Y.; He, B.; Wang, R.; Ling, Y.; Zhao, L. Effect of Co doping on sinterability and protonic conductivity of BaZr_{0.1}Ce_{0.7}Y_{0.1}Yb_{0.1}O_{3-δ} for protonic ceramic fuel cells. *J. Power Sources* **2017**, *347*, 14–20. [[CrossRef](#)]
68. Dailly, J.; Taillades, G.; Ancelin, M.; Pers, P.; Marrony, M. High performing BaCe_{0.8}Zr_{0.1}Y_{0.1}O_{3-δ}–Sm_{0.5}Sr_{0.5}CoO_{3-δ} based protonic ceramic fuel cell. *J. Power Sources* **2017**, *361*, 221–226. [[CrossRef](#)]
69. Ding, H.; Xue, X. GdBa_{0.5}Sr_{0.5}Co₂O_{5+δ} layered perovskite as promising cathode for proton conducting solid oxide fuel cells. *J. Alloys Compd.* **2010**, *496*, 683–686. [[CrossRef](#)]
70. Shi, H.; Ding, Z.; Ma, G. Electrochemical performance of cobalt-free Nd_{0.5}Ba_{0.5}Fe_{1-x}Ni_xO_{3-δ} cathode materials for intermediate temperature solid oxide fuel cells. *Fuel Cells* **2016**, *16*, 258–262. [[CrossRef](#)]
71. Dailly, J.; Ancelin, M.; Marrony, M. Long term testing of BCZY-based protonic ceramic fuel cell PCFC: Micro-generation profile and reversible production of hydrogen and electricity. *Solid State Ionics* **2017**, *306*, 69–75. [[CrossRef](#)]
72. Lee, S.; Park, S.; Wee, S.; Baek, H.; Shin, D. One-dimensional structured La_{0.6}Sr_{0.4}Co_{0.2}Fe_{0.8}O_{3-δ}–BaCe_{0.5}Zr_{0.35}Y_{0.15}O_{3-δ} composite cathode for protonic ceramic fuel cells. *Solid State Ionics* **2018**, *320*, 347–352. [[CrossRef](#)]
73. Amiri, T.; Singh, K.; Sandhu, N.K.; Hanifi, A.R.; Etsell, T.H.; Luo, J.-L.; Thangadurai, V.; Sarkar, P. High performance tubular solid oxide fuel cell based on Ba_{0.5}Sr_{0.5}Ce_{0.6}Zr_{0.2}Gd_{0.1}Y_{0.1}O_{3-δ} proton conducting electrolyte. *J. Electrochem. Soc.* **2018**, *165*, F764–F769. [[CrossRef](#)]
74. Li, F.; Tao, Z.; Dai, H.; Xi, X.; Ding, H. A high-performing proton-conducting solid oxide fuel cell with layered perovskite cathode in intermediate temperatures. *Int. J. Hydrogen Energy* **2018**, *43*, 19757–19762. [[CrossRef](#)]
75. Lyagaeva, J.; Danilov, N.; Tarutin, A.; Vdovin, G.; Medvedev, D.; Demin, A.; Tsiakaras, P. Designing a protonic ceramic fuel cell with novel electrochemically active oxygen electrodes based on doped Nd_{0.5}Ba_{0.5}FeO_{3-δ}. *Dalton Trans.* **2018**, *47*, 5149–8157. [[CrossRef](#)] [[PubMed](#)]
76. Lyagaeva, J.; Vdovin, G.; Hakimova, L.; Medvedev, D.; Demin, A.; Tsiakaras, P. BaCe_{0.5}Zr_{0.3}Y_{0.2-x}Yb_xO_{3-δ} proton-conducting electrolytes for intermediate-temperature solid oxide fuel cells. *Electrochim. Acta* **2017**, *251*, 554–561. [[CrossRef](#)]

77. Gui, L.; Ling, Y.; Li, G.; Wang, Z.; Wan, Y.; Wang, R.; He, B.; Zhao, L. Enhanced sinterability and conductivity of $\text{BaZr}_{0.3}\text{Ce}_{0.5}\text{Y}_{0.2}\text{O}_{3-\delta}$ by addition of bismuth oxide for proton conducting solid oxide fuel cells. *J. Power Sources* **2016**, *301*, 369–375. [[CrossRef](#)]
78. Zhang, L.; Li, C. $\text{BaFe}_{0.6}\text{Co}_{0.3}\text{Ce}_{0.1}\text{O}_{3-\delta}$ as cathode materials for proton-conducting solid oxide fuel cells. *Ceram. Int.* **2016**, *42*, 10511–10515. [[CrossRef](#)]
79. Danilov, N.A.; Tarutin, A.P.; Lyagaeva, J.G.; Pikalova, E.Y.; Murashkina, A.A.; Medvedev, D.A.; Patrakeev, M.V.; Demin, A.K. Affinity of $\text{YBaCo}_4\text{O}_{7+\delta}$ -based layered cobaltites with protonic conductors of cerate-zirconate family. *Ceram. Int.* **2017**, *43*, 15418–15423. [[CrossRef](#)]
80. Danilov, N.; Pikalova, E.; Lyagaeva, J.; Antonov, B.; Medvedev, D.; Demin, A.; Tsiakaras, P. Grain and grain boundary transport in $\text{BaCe}_{0.5}\text{Zr}_{0.3}\text{Ln}_{0.2}\text{O}_{3-\delta}$ (Ln-Y or lanthanide) electrolytes attractive for protonic ceramic fuel cells application. *J. Power Sources* **2017**, *366*, 161–168. [[CrossRef](#)]



© 2018 by the authors. Licensee MDPI, Basel, Switzerland. This article is an open access article distributed under the terms and conditions of the Creative Commons Attribution (CC BY) license (<http://creativecommons.org/licenses/by/4.0/>).